

## GEOLOGY

## Abundant off-fault seismicity and orthogonal structures in the San Jacinto fault zone

Zachary E. Ross,<sup>1\*</sup> Egill Hauksson,<sup>1</sup> Yehuda Ben-Zion<sup>2</sup>

The trifurcation area of the San Jacinto fault zone has produced more than 10% of all earthquakes in southern California since 2000, including the June 2016  $M_w$  (moment magnitude) 5.2 Borrego Springs earthquake. In this area, the fault splits into three subparallel strands and is associated with broad  $V_p/V_s$  anomalies. We synthesize spatiotemporal properties of historical background seismicity and aftershocks of the June 2016 event. A template matching technique is used to detect and locate more than 23,000 aftershocks, which illuminate highly complex active fault structures in conjunction with a high-resolution regional catalog. The hypocenters form dipping seismicity lineations both along strike and nearly orthogonal to the main fault, and are composed of interlaced strike-slip and normal faults. The primary faults change dip with depth and become listric by transitioning to a dip of  $\sim 70^\circ$  near a depth of 10 km. The  $M_w$  5.2 Borrego Springs earthquake and past events with  $M > 4.0$  occurred on the main faults, whereas most of the low-magnitude events are located in a damage zone (several kilometers wide) at seismogenic depths. The lack of significant low-magnitude seismicity on the main fault traces suggests that they do not creep. The very high rate of aftershocks likely reflects the large geometrical fault complexity and perhaps a relatively high stress due to a significant length of time elapsed since the last major event. The results provide important insights into the physics of faulting near the brittle-ductile transition.

## INTRODUCTION

The San Jacinto fault zone (SJFZ) is the most seismically active fault system in the southern California plate boundary, having produced 11 earthquakes with  $M$  (magnitude)  $> 6.0$  in the last 120 years (1). The SJFZ includes several right-lateral strike-slip faults that exhibit notable heterogeneity in fault geometry along strike, as measured from surface geology, geodesy, seismicity, and focal mechanisms (2–5). A segment in the central region referred to as the Anza seismic gap (4) lacks microseismicity and has not produced a major earthquake in the last 200 years (6). Southeast of the Anza gap, the SJFZ splits into three subparallel strands called the Coyote Creek (CC), Clark (CL), and Buck Ridge (BR) faults (Fig. 1). This comparatively small region, which is often referred to as the trifurcation area, is responsible for more than 10% of all earthquakes produced in southern California since 2000. During this period, 10 separate events with  $M > 4.0$  have occurred (blue focal mechanisms), and all have right-lateral strike-slip mechanisms. The elevated rate of earthquakes across the whole SJFZ (compared to the San Andreas fault) has been suggested to be driven by deep creep (7), but this does not explain the considerable heterogeneity in seismicity rates along strike or why the trifurcation area is very seismically active.

Some of the highest-resolution information on the internal properties of fault zone structures comes from fault zone head and trapped waves that propagate along bimaterial interfaces and coherent low-velocity damage zones (8–10). Fault zone trapped waves were observed at several sites along the CC, CL, and BR faults (11–13) and were used to infer the presence of  $\sim 150$ -m-wide core damage zones in the upper 4 to 5 km. Recent local earthquake tomography focusing on the trifurcation area indicates the existence of bimaterial interfaces along all the three main faults and a broad damage zone throughout the region in the upper 5 km (14). Such damage zones typically consist of hierarchical networks of faults and cracks that evolve with the ongoing deformation in the region (15). Wechsler *et al.* (16) documented pulverized and damaged rocks in the trifurcation area and observed larger rock damage

near geometric complexities and areas between parallel fault segments. Between the CC and CL faults, there are listric normal faults oriented orthogonal to the main fault traces (17), which are likely formed from local extension produced by subparallel slip on CC and CL. Although these studies provide useful insight into the internal structure and mechanics of the SJFZ, they are restricted to shallow depths above the seismogenic zone. Analysis of seismicity can illuminate fault zone structures at seismogenic depths (18, 19). Several studies examined lineations in seismicity for different areas of the SJFZ and found that many structures dip to the northeast (4, 19).

On 10 June 2016, the  $M_w$  (moment magnitude) 5.2 Borrego Springs earthquake occurred on the CL fault, generating more than 1500 aftershocks over a span of 2 weeks that were detected with standard procedures. Here, we use a template matching technique to detect and locate more than 23,000 additional aftershocks to probe the internal structure of the fault at seismogenic depths. The hypocenters of these aftershocks are examined in conjunction with a high-resolution regional catalog (20) to better understand the relationship between seismicity rates and fault zone structures.

## RESULTS

Figure 1 shows the locations of 9891 aftershocks alongside the relocated seismicity from 1981 to the present (black dots). While a few aftershocks (colored dots) occurred on the CL fault itself, most events were generated in a broad region between the CL and BR faults. The newly detected aftershocks are highly clustered in space and delineate numerous structures that are not resolvable from the network catalog alone. Closer examination reveals lineations with a range of length scales oriented nearly orthogonal to the main structures (inset). Several of the largest seismicity clusters trending in a northeast direction appear to have been activated for the first time in at least 35 years. They are composed of events with diverse focal mechanisms, including right-lateral strike-slip, normal, and, to a lesser extent, reverse faulting. This behavior is notable because in May 2008, a pair of  $M$  4.1 and  $M$  4.2 events occurred in almost the same location as the 2016 main shock but did not trigger similar seismicity that was detected by the regional network. Of the nine aftershocks in the 2016 sequence with  $M > 3.0$ , more

2017 © The Authors, some rights reserved; exclusive licensee American Association for the Advancement of Science. Distributed under a Creative Commons Attribution NonCommercial License 4.0 (CC BY-NC).

<sup>1</sup>Seismological Laboratory, California Institute of Technology, Pasadena, CA 91125, USA. <sup>2</sup>Department of Earth Sciences, University of Southern California, Los Angeles, CA 90089, USA.

\*Corresponding author. Email: zross@gps.caltech.edu

than half are normal faulting. Such diversity in focal mechanisms is observed across the entire aftershock data set as well as in a previous focal mechanism catalog for the same area (5, 21).

To better understand the relationship between the seismicity and the three main faults, we examined the hypocenters as a function of depth. Figure 2 shows a fault-normal cross section (A–A'), containing all events within 5 km of the profile. Numerous structures are delineated in the seismicity, including several that dip toward the northeast. Dashed lines indicate the most likely positions of the fault planes for CC, CL, and BR at these depths. These positions were determined by the locations of the 2008  $M_w$  4.1, 2010  $M_w$  5.4, 2013  $M_w$  4.7, and 2016  $M_w$  5.2 events together with their focal mechanisms and nearby lineations of seismicity. Additional significant lineations are visible and are likely minor fault strands. The CL, CC, and BR faults appear to dip  $\sim 70^\circ$  to the northeast below a depth of about 10 km. The measured dip angles are in agreement with the focal mechanisms of several events with  $M > 4.0$ . If these dip angles are correct, the faults must be listric and transition to a near-vertical orientation at a depth of approximately 10 to 13 km; otherwise, they would intersect the surface several kilometers to the southwest of the surface traces, which is unlikely. An additional line of evidence for this transitional behavior is that the lineations and focal mechanisms in the upper 6 to 10 km are markedly more vertical than those in between depths of 10 and 16 km. The aftershocks of the 2016 Borrego Springs earthquake primarily occupy the region between the CL and BR faults (red dots). Similar to the historical seismicity, they also demonstrate faint but persistent lineations dipping at  $\sim 70^\circ$ .

In Fig. 3, we show the seismicity along a fault-parallel cross section (B–B'). In contrast to the fault-normal profile, relatively few narrow lineations are visible in the seismicity, but there are numerous clusters

among the detected aftershocks (red dots). Some of these structures are associated with normal and left-lateral strike-slip faults, whereas others are just parts of right-lateral surfaces. The largest aftershock ( $M$  3.8) occurred near the 10-km distance mark along strike. The rupture plane is well resolved and dips toward the southeast, in agreement with the normal faulting mechanism. Several steeply dipping structures located between the CL and BR faults are visible at shallower depths. Many of the structures are coincident with the right-lateral faults in Fig. 2, which require that they are orthogonal to each other (Fig. 1, inset). Several previous studies identified earthquakes with rupture directivities to the northeast and northwest (22–24), and these events can be tied to these specific fault structures.

Focal mechanisms for more than 400 aftershocks of the 2016 Borrego Springs sequence exhibit unusual diversity between the CL and BR faults on a scale of  $\sim 100$  m (Fig. 4). This complex pattern points to a broad, active damage zone between the CL and BR faults consisting of interlaced faults and cracks of various lengths. These focal mechanisms are generally right-lateral strike-slip in seismic lineations parallel to the SJFZ and normal or left-lateral faulting in clusters oriented fault-perpendicular. Although the damage zone produces most of the seismicity in the trifurcation area, it has not produced an earthquake with  $M > 4.0$  since at least 2001. This is in contrast to the three main strands of the SJFZ that produced 10 separate main shock events with  $M > 4.0$  during this period. The network of fine structures is strongly asymmetric to the northeast side of the CL fault. This pronounced damage asymmetry is also seen in the geomorphology (16) and anomalous  $V_p/V_s$  values (14) and, on a smaller scale, in geological mapping of rock damage at the surface (25) and in a 100- to 200-m-wide seismic trapping structure (12, 13). The pronounced active structure about halfway between CL and BR (oriented fault-parallel) may indicate an unknown major fault strand or it could be

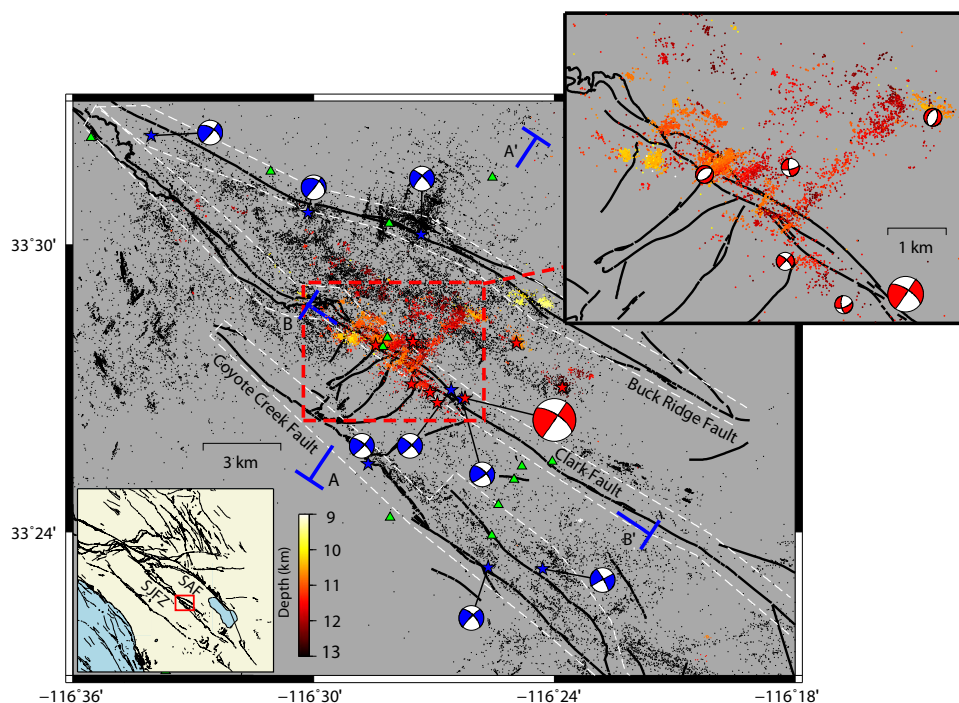


**Fig. 1. Map of the trifurcation area of the SJFZ.** Historical seismicity is denoted by black dots (20). Events with  $M > 4.0$  that have occurred in this area since 2001 are indicated by blue stars and focal mechanisms. Aftershocks of the 2016 Borrego Springs earthquake are colored by depth. Red stars and focal mechanisms indicate aftershocks with  $M > 3.0$ . Stations used are denoted by green triangles. The inset contains a close-up of the detected aftershocks, which delineate numerous strike-slip and normal faults in conjugate orientations. Profiles of seismicity along cross sections A–A' and B–B' are shown in Figs. 2 and 3. SAF, San Andreas fault.

an edge to the active damage zone. This structure coincides with a horizontal  $V_P/V_S$  signature in the tomographic model of Allam *et al.* (14).

With a more complete picture of the internal structure of the SJFZ at depth, it can now be compared with historical seismicity patterns. Within the trifurcation area, the three main faults have produced  $M > 4.0$  earthquakes on average every 2.2 years but generated only a few small events on the faults themselves. The damage zone between the CL and BR faults has produced microearthquakes daily but no  $M > 4.0$  earthquakes in at least 16 years. To further investigate this behavior, we divided the relocated network catalog from 1981 to the present into on-fault and off-fault groups. The on-fault events are defined to be within the white dashed regions surrounding the three main faults in Fig. 1, which are generally within 1 km of the surface traces; all remaining events that do not occur on the primary structures are considered off-fault.

The on-fault events clearly have a frequency-magnitude distribution that is different from that of the off-fault events (Fig. 5). Widening the on-fault regions by twice as much leads to essentially the same results. The  $b$

values calculated with the maximum likelihood method (26) for the on-fault and off-fault events are  $1.15 \pm 0.10$  and  $1.31 \pm 0.07$ , respectively, indicating that the two groups are statistically different. Here,  $M 2.0$  is taken as the completeness magnitude based on visual inspection. Because these regions are volumes, rather than surfaces, the on-fault event distribution contains a significant number of events produced from structures other than the primary interfaces. This is most clearly seen by the marked change in slope of the on-fault events around  $M 3.0$ . For the on-fault events with  $M > 3.0$  only, the  $b$  value is  $0.77 \pm 0.25$ , which is significantly lower than the  $b$  value for all on-fault events together. If the true rate of on-fault earthquakes is characterized by this  $b$  value (0.77), then this implies that only about 2% of all earthquakes in the trifurcation area were generated on the primary fault interfaces. Thus, the few earthquakes produced on the fault, which include all of the largest events, form a distinctly different population from the off-fault events. This is consistent with the notion that large faults have frequency-magnitude statistics different from those of small faults, and that a broad power law distribution is produced in part by regional averaging (27).

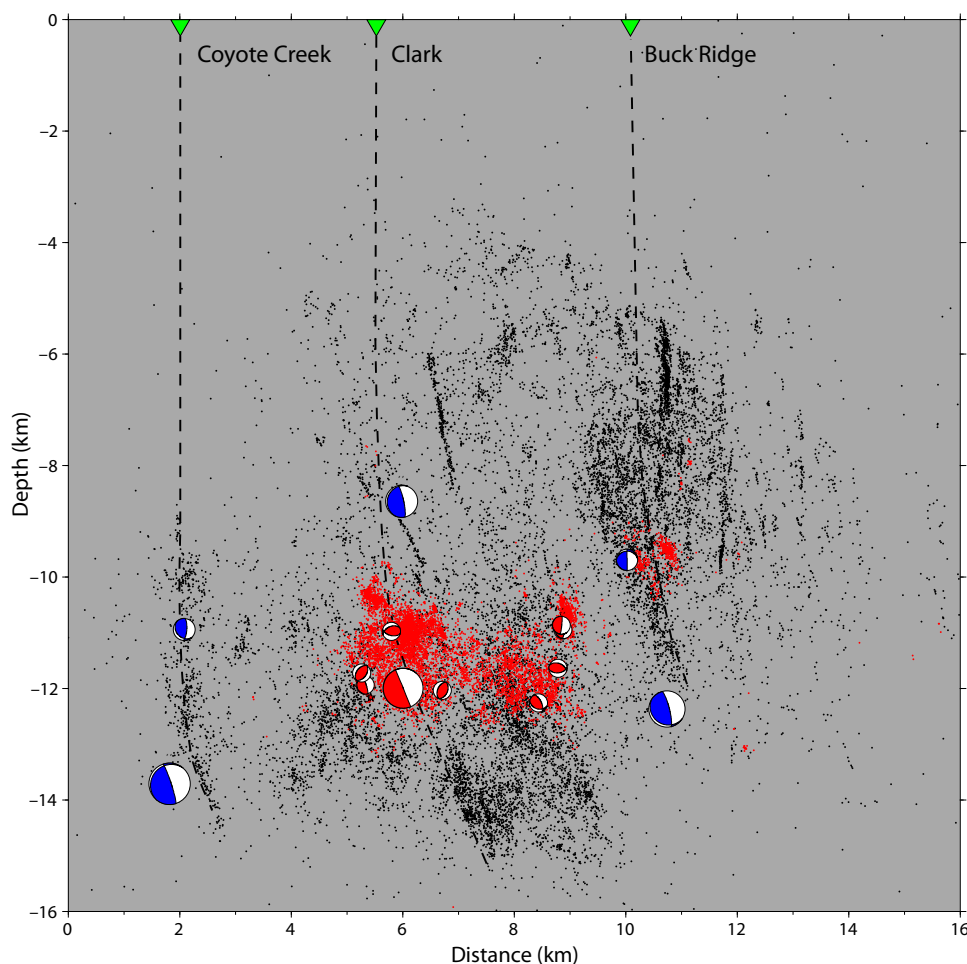


**Fig. 2. Fault-normal cross section A–A' detailing seismicity within 5 km.** Black dots denote the regional network relocated solutions (20), whereas red dots indicate the detected aftershocks of the 2016 Borrego Springs earthquake. Red focal mechanisms correspond to aftershocks with  $M > 3.0$ , whereas blue focal mechanisms on the CL, CC, and BR faults are from the 2008  $M_w$  4.06, 2010  $M_w$  5.4, and 2013  $M_w$  4.7 sequences, respectively. The 2016 main shock is indicated by the largest red focal mechanism. All focal mechanisms shown are rear hemisphere projections. The interpreted locations of the CC, CL, and BR fault planes are shown as dashed lines and dip nearly  $70^\circ$  below 10 km. A change in dip must occur at around 10 to 13 km in order for the faults to meet with the surface expression (green triangles). In the regions off the main faults, there are damage zones with intense distributed seismicity that includes persistently dipping lineations.

## DISCUSSION

In Fig. 6, we provide a schematic representation of the results. The CC, CL, and BR faults are all listric, right-lateral strike-slip faults capable of producing large events, which are nearly vertical in the top 10 to 12 km and transition rather abruptly to a dip of roughly 70°. A broad damage zone exists across the trifurcation area in the top 5 km and is associated with the ongoing regional deformation, producing abundant complex microseismicity. Several normal faults exist between the CC and CL faults and are oriented perpendicular to the strike of the SJFZ. Between the CL and BR faults at a depth of 8 to 16 km, there is a younger, seismically active damage zone consisting of interlaced strike-slip and normal faults.

A general increase in  $b$  value with distance away from major faults was previously observed for the whole of southern California (28). Different  $b$  values were also observed between large and small faults within a swarm in the Long Valley Caldera (29). They found that the  $b$  value increased with elapsed time from the start of the swarm and concluded that these variations were the result of both limitations on the maximum magnitude for the smaller faults as well as a more heterogeneous stress field at the smaller scale. These observations are generally similar to our observations in the SJFZ. The clear contrast in seismicity rate

between the damage zone and main faults is seen not just within the 2016 Borrego Springs sequence but also over the entire 35-year catalog for the region.

Earthquake hypocenters play a key role in this study, and it is important to discuss their accuracy. The relocated regional seismicity catalog is estimated to have relative errors of 100 m and absolute errors of 0.8 to 1.5 km (20). For the 2016 Borrego Springs sequence, 95% of the relative errors are less than 150 m (horizontal) and 162 m (vertical), which is similar in quality to previous studies using template matching (29, 30). Thus, the conclusions drawn from seismicity structures should not be affected by the resolution of the relative location errors. However, the less-resolved absolute position of the entire cloud of events results in additional uncertainty over where the dip transitions occur. In addition, velocity contrasts have been observed along all of these faults in the upper ~7 km (14, 31, 32), which have been shown to add absolute error in the form of a lateral shift if unaccounted for (33). We used a high-quality three-dimensional (3D) velocity model for southern California in the relocation process (34), which should help minimize possible biases introduced by near-source velocity heterogeneity. The hypoDD method (35) should further help mitigate the effects of 3D structure along the path. The dipping at depth is unlikely to result from

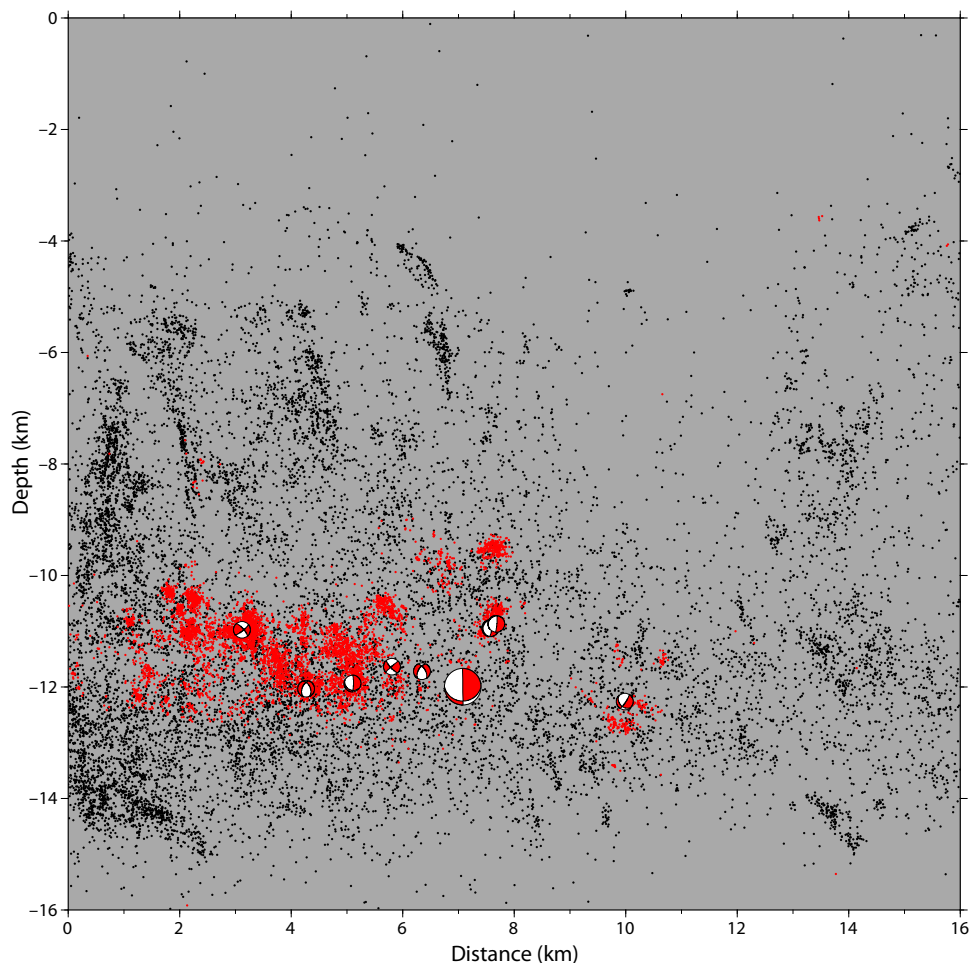


**Fig. 3. Fault-parallel cross section B-B' detailing all seismicity within 5 km.** Black dots denote the regional network relocated solutions (20), whereas red dots indicate the detected aftershocks of the 2016 Borrego Springs earthquake. Red focal mechanisms correspond to aftershocks with  $M > 3.0$ . All focal mechanisms shown are rear hemisphere projections. Numerous dipping structures are visible and are generally normal faulting or left-lateral strike-slip. Focal mechanisms correspond to 2016 aftershocks with  $M > 3.0$ . The 2016 Borrego Springs main shock is indicated by the largest focal mechanism.



velocity contrasts because they decrease with depth (36, 37). Further, similar dipping behavior is not seen at the Parkfield section of the San Andreas fault, which has a stronger velocity contrast than the study area (10, 38).

Several previous studies claimed that the SJFZ may be dipping toward the northeast. Lindsey *et al.* (39) used a model with a single plane and constant dip to fit geodetic data in the central section of the SJFZ and concluded that it dips 80° to 85°. Given the model simplicity, the

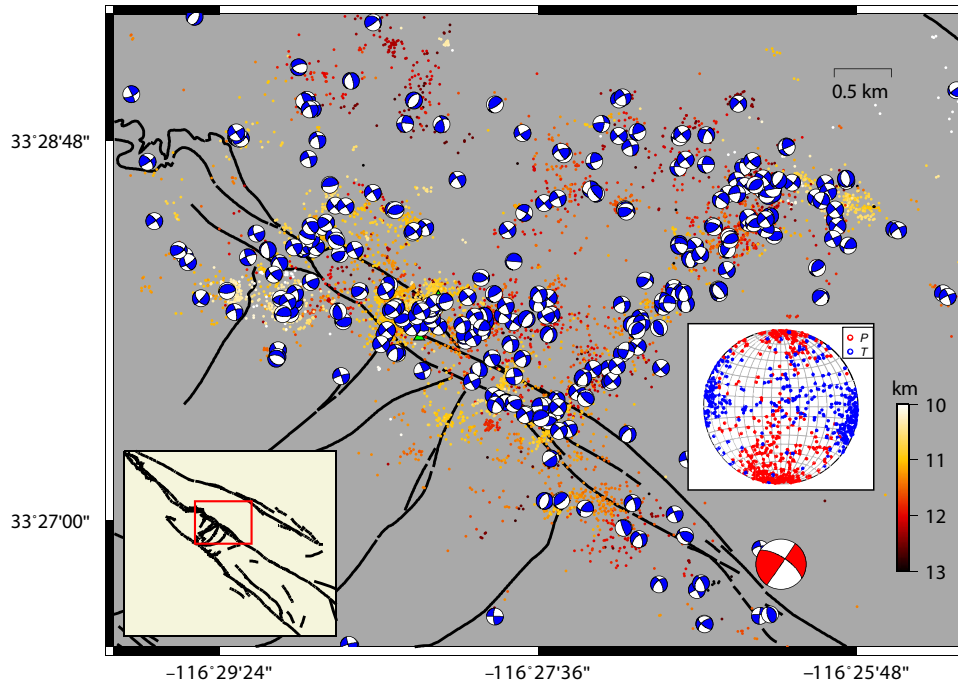


**Fig. 4. Aftershock focal mechanisms.** Most cases are either strike-slip or normal faulting. The diversity of focal mechanisms is observed on a scale of ~100 m. Structures that are oriented fault-normal are typically normal faulting or left-lateral strike slip, whereas fault-parallel events are typically right-lateral strike-slip. Seismicity is colored by depth, according to the scale. Stereonet shows *P* and *T* axes of all focal mechanisms. The inset indicates the map's location within the broader trifurcation area.

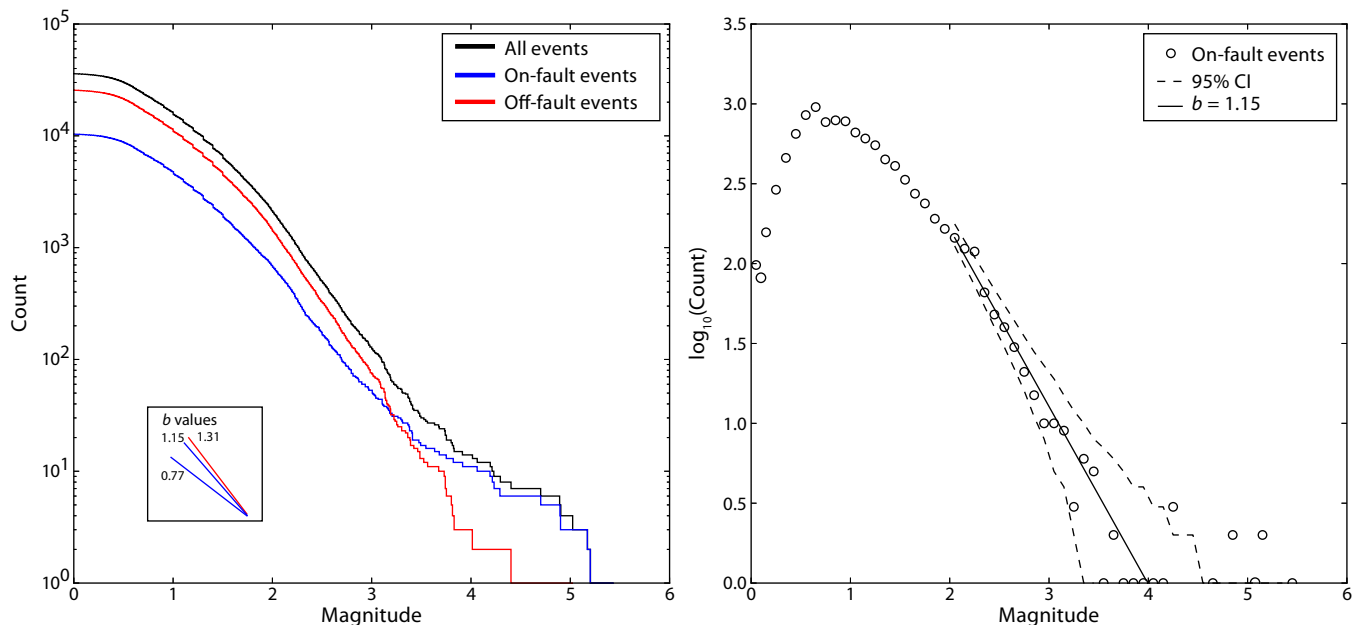


**Fig. 5. Frequency-magnitude distributions of on-fault and off-fault events since 1981.** The regions for on-fault events are defined by the white dashed lines in Fig. 1. The left panel presents cumulative statistics for various event populations, whereas the right panel shows discrete statistics for on-fault events and the 95% confidence interval (CI). The largest events occur only on the main faults, whereas nearly two-thirds of all events occur off-fault. On-fault events have a *b* value of  $1.15 \pm 0.10$ , whereas off-fault events have a *b* value of  $1.31 \pm 0.07$ . On-fault events with  $M > 3.0$  have a distinctly different *b* value ( $0.77 \pm 0.25$ ), forming a separate population. These observations suggest that many events are produced on off-fault structures even within the defined on-fault regions and that the primary fault interfaces are likely to be locked. On-fault events with  $M > 4.0$  are outside the 95% CI in the discrete statistics shown in the right panel.

inferred values are similar to what would be obtained by averaging our fault geometry over the top 16 km. The Southern California Earthquake Center Community Fault Model has average dips of 89°, 86°, and 89° for the CC, CL, and BR faults, respectively (40). Lineations across the entire SJFZ were previously examined by Nemser and Cowan (19), who concluded that the main fault strands exhibit down-dip segmentation, as seen in shallow, porous sedimentary rocks. Such rocks produce compaction bands during failure, which lead to hardening and delocalization. However, the low-porosity igneous rocks that exist at depth in the trifurcation area tend to fail in a weakening process leading to localization (41–43). The more recent 2010  $M_w$  5.4, 2013  $M_w$  4.7, and 2016  $M_w$  5.2 events on the CC, BR, and CL faults, respectively, indicate that moderate events in the area tend to occur on localized faults (Fig. 2). It is more plausible that the fault segments identified are essentially collections of cracks within a broad damage zone (15). Because no earthquake has ruptured the entire seismogenic zone of the central SJFZ in more than half a century, the small events produced in the interseismic period are generally insufficient to investigate whether a primary fault plane exists at depth.

Along the strike of the SJFZ, there are significant spatial fluctuations in the observed seismicity rates. The most extreme example of this behavior is between the trifurcation area and the Anza gap immediately to the northwest, which has the lowest rate of earthquakes in the SJFZ (4). This segment of the fault, which is a 20-km-long linear strand that is highly localized, also has the simplest geometry in the entire SJFZ (25). Paleoseismic studies indicate that the Anza segment had numerous previous large events ( $M_w \sim 7.3$ ), with a recurrence interval estimated at 254 years (6). The lack of microseismicity is most likely related to the geometrical simplicity of that segment and the fewer

off-fault structures as compared with the trifurcation area. Other factors, such as possibly higher frictional strength or lack of fluids, may also play a role. The considerably higher rate of seismicity in the trifurcation area, including numerous events with  $M > 4.0$ , increases the loading on the Anza segment and the likelihood of a future large SJFZ event.

The relative geometric simplicity of the main faults and larger available surface area allow for larger events to occur, with focal mechanisms typically well aligned with the regional stress field. The alignments of seismicity and the focal mechanisms of events with  $M > 4.0$  suggest that the main faults become listric near a depth of 10 km. On the other hand, the damage zone has a complex distribution of cracks with different sizes that preferentially produce smaller events with diverse focal mechanisms (Fig. 4). These cracks extend down to the brittle-ductile transition zone, are often aligned with the regional stress field, and have a conjugate alignment nearly orthogonal to the main direction of the SJFZ. Geometric complexity produces stress concentrations that lead to increased low-magnitude seismicity (27) and, given the highly complex structures observed within the trifurcation area, provides a clear explanation for the anomalously high seismicity rates. Although the SJFZ has long been known as the most active fault zone in southern California, these observations indicate that most of the activity is off-fault and that the primary fault interfaces are likely to be locked.

A number of mechanisms may produce the complex off-fault structures. These include weak dependence of strength on normal stress, ductile shear zones at depth driving deformation in the brittle crust (44), block rotation between master faults (45), reactivation of a rifting system in compressive stress (46), or high-angle branching near the terminus of large earthquake ruptures (47). The high-resolution images of these structures provide important insights into the physics of faulting at depth. The relative proximity of the trifurcation area to rifting in the Gulf of California and Salton Trough, its association with several major fault branches, the relatively large average hypocenter depth, and occasional large earthquake ruptures suggest that all these mechanisms may be responsible for the generation and evolution of the observed complex seismicity structures. The most likely mechanism affecting the current deep orthogonal seismicity (Fig. 1) may be loading from an ongoing ductile deformation with similar orientation below the seismogenic zone.

## MATERIALS AND METHODS

### Data

We used seismic data from 19 three-component broadband and short-period seismometers within 20 km of the main shock (48) for the period 9 June 2016 to 24 June 2016. The used stations are from the CI, AZ, PB, SB, and YN networks. A total of 1580 earthquakes were detected and located by the Southern California Seismic Network (SCSN) during the period. SCSN analysts made the  $P$ - and  $S$ -wave arrival picks.

### Template relocation

We relocated the 1580 aftershocks using a waveform cross-correlation method (20), with the intent of using their waveforms as templates for detecting additional earthquakes. The differential times measured during this process were used with the hypoDD algorithm (35) to obtain high-quality hypocenters and origin times. The new template locations were also used to determine more accurate focal mechanisms from first-motion polarities and  $S$ -to- $P$  amplitude ratios (21). A total of 412 solutions had a quality of A or B, as determined by the Hash algorithm (49), which are the focal mechanisms used in this study.

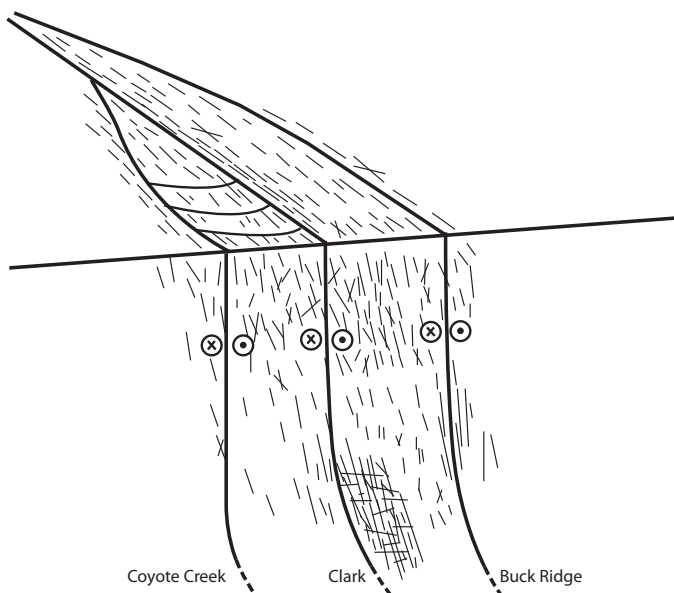


**Fig. 6. Schematic of the SJFZ trifurcation area.** Three main right-lateral strike-slip faults are near vertical in the upper 10 km and dip roughly 70° below this depth. In the top 5 km, there is a broad damage zone associated with the ongoing regional deformation. Between the CL and BR faults, there is a seismically active damage zone at depth consisting of interlaced normal and strike-slip faults. The damage zone produces most of the earthquakes in the region and appears to terminate roughly halfway between CL and BR.

## Event detection using template matching

We used a matched filter method (29) to detect additional earthquakes in the continuous data. The method is briefly summarized for clarity. Data were first band-pass-filtered between 2 and 15 Hz. Template waveforms were constructed using a 2.5-s window for *P* waves and a 4.0-s window for *S* waves on all three components for each template event. These windows were chosen to start 0.2 s before the analysts pick. For source-receiver combinations with *S-P* times of less than 2.5 s, the *P*-wave window was shortened to the *S-P* time to ensure no overlap with the *S* wave. The template windows were then correlated against 24-hour continuous data at a time. Each cross-correlation function was shifted back in time by an amount equal to the observed travel time of the template and summed across all phases, channels, and stations. Detections were made using a threshold of eight times the median absolute deviation for the respective day. We then measured the differential times from the individual cross-correlation functions for each respective phase and station using a threshold of seven times the median absolute deviation. Both negative and positive correlation values were used, and differential times were interpolated to subsample precision. This process was then repeated for all template events, and detections that were spaced less than 2 s apart were linked to identify the best-matching template. For each detection chain, the template with the largest average cross-correlation coefficient was selected, and its location was assigned to the detected event. Applying this procedure resulted in 25,392 detected events and 28 million differential times, including the 1580 template events. Magnitudes were calculated by using only phases with measured differential times. For these phases, peak amplitude ratios were calculated between the detected phase and the template phase. The final magnitude estimate was formed by taking the median over all amplitude ratios and assuming that a factor of 10 in amplitude corresponds to one magnitude unit difference (50). The differential times were then used as the input for hypoDD (35), resulting in 9891 events with at least 20 total phases surviving. For the relocation process, we used the 3D velocity model of Fang *et al.* (34). These events were used throughout the paper. Additional details regarding the detected events are given in the Supplementary Materials.

## Location error estimation

We used a resampling technique to estimate the relative errors of the locations for the 2016 Borrego Springs sequence (51). For this procedure, we randomly sampled 90% of the event pairs and used these values as new inputs to the hypoDD program. This process was repeated for a total of 1000 iterations to quantify the variability in latitude, longitude, and depth for each event. The final error estimates for each event were determined from the 95% CIs of each respective parameter.

## SUPPLEMENTARY MATERIALS

Supplementary material for this article is available at <http://advances.sciencemag.org/cgi/content/full/3/3/e1601946/DC1>

fig. S1. Additional details regarding the detected 2016 Borrego Springs aftershocks.

fig. S2. Cross section along profile A-A'.

fig. S3. Map of seismic stations used.

data set S1. Seismicity catalog of all detections (unrelocated).

data set S2. Seismicity catalog of hypoDD relocated detections.

movie S1. Animation of the relocated seismicity in 3D.

## REFERENCES AND NOTES

1. Y. Y. Kagan, D. D. Jackson, Y. Rong, A new catalog of southern California earthquakes, 1800-2005. *Seismol. Res. Lett.* **77**, 30–38 (2006).
2. T. Rockwell, C. Loughman, P. Merifield, Late quaternary rate of slip along the San Jacinto Fault Zone near Anza, southern California. *J. Geophys. Res.* **95**, 8593–8605 (1990).
3. Y. Fialko, Interseismic strain accumulation and the earthquake potential on the southern San Andreas fault system. *Nature* **441**, 968–971 (2006).
4. C. O. Sanders, H. Kanamori, A seismotectonic analysis of the Anza seismic gap, San Jacinto Fault Zone, southern California. *J. Geophys. Res.* **89**, 5873–5890 (1984).
5. I. W. Bailey, Y. Ben-Zion, T. W. Becker, M. Holschneider, Quantifying focal mechanism heterogeneity for fault zones in central and southern California. *Geophys. J. Int.* **183**, 433–450 (2010).
6. T. K. Rockwell, T. E. Dawson, J. Y. Ben-Horin, G. Seitz, A 21-event, 4,000-year history of surface ruptures in the Anza Seismic gap, San Jacinto Fault, and implications for long-term earthquake production on a major plate boundary fault. *Pure Appl. Geophys.* **172**, 1143–1165 (2015).
7. S. Wdowinski, Deep creep as a cause for the excess seismicity along the San Jacinto fault. *Nat. Geosci.* **2**, 882–885 (2009).
8. Y. Ben-Zion, K. Aki, Seismic radiation from an *SH* line source in a laterally heterogeneous planar fault zone. *Bull. Seismol. Soc. Am.* **80**, 971–994 (1990).
9. Y.-G. Li, P. Leary, K. Aki, P. Malin, Seismic trapped modes in the Oroville and San Andreas fault zones. *Science* **249**, 763–766 (1990).
10. Y. Ben-Zion, P. Malin, San Andreas fault zone head waves near Parkfield, California. *Science* **251**, 1592–1594 (1991).
11. Y.-G. Li, F. L. Vernon, Characterization of the San Jacinto fault zone near Anza, California, by fault zone trapped waves. *J. Geophys. Res.* **106**, 30671–30688 (2001).
12. M. A. Lewis, Z. Peng, Y. Ben-Zion, F. L. Vernon, Shallow seismic trapping structure in the San Jacinto fault zone near Anza, California. *Geophys. J. Int.* **162**, 867–881 (2005).
13. Z. E. Ross, Y. Ben-Zion, An algorithm for automated identification of fault zone trapped waves. *Geophys. J. Int.* **202**, 933–942 (2015).
14. A. A. Allam, Y. Ben-Zion, I. Kurzon, F. Vernon, Seismic velocity structure in the Hot Springs and Trifurcation areas of the San Jacinto fault zone, California, from double-difference tomography. *Geophys. J. Int.* **198**, 978–999 (2014).
15. Y. Ben-Zion, C. G. Sammis, Characterization of fault zones. *Pure Appl. Geophys.* **160**, 677–715 (2003).
16. N. Wechsler, T. K. Rockwell, Y. Ben-Zion, Application of high resolution DEM data to detect rock damage from geomorphic signals along the central San Jacinto Fault. *Geomorphology* **113**, 82–96 (2009).
17. R. V. Sharp, En echelon fault patterns of the San Jacinto fault zone, in vol. 118 of *San Andreas Fault in Southern California: A Guide to San Andreas Fault from Mexico to Carrizo Plain*, J. C. Cromwell, Ed. (California Division of Mines and Geology, 1975), pp. 147–154.
18. A. M. Rubin, Aftershocks of microearthquakes as probes of the mechanics of rupture. *J. Geophys. Res.* **107**, ESE 3-1–ESE 3-16 (2002).
19. E. S. Nemes, D. S. Cowan, Downdip segmentation of strike-slip fault zones in the brittle crust. *Geology* **37**, 419–422 (2009).
20. E. Hauksson, W. Yang, P. M. Shearer, Waveform relocated earthquake catalog for southern California (1981 to June 2011). *Bull. Seismol. Soc. Am.* **102**, 2239–2244 (2012).
21. W. Yang, E. Hauksson, P. M. Shearer, Computing a large refined catalog of focal mechanisms for southern California (1981–2010): Temporal stability of the style of faulting. *Bull. Seismol. Soc. Am.* **102**, 1179–1194 (2012).
22. J. Mori, Fault plane determinations for 3 small earthquakes along the San Jacinto fault, California: Search for cross faults. *J. Geophys. Res.* **98**, 17711–17722 (1993).
23. I. Kurzon, F. L. Vernon, Y. Ben-Zion, G. Atkinson, Ground motion prediction equations in the San Jacinto Fault Zone: Significant effects of rupture directivity and fault zone amplification. *Pure Appl. Geophys.* **171**, 3045–3081 (2014).
24. Z. E. Ross, Y. Ben-Zion, Toward reliable automated estimates of earthquake source properties from body wave spectra. *J. Geophys. Res.* **121**, 4390–4407 (2016).
25. O. Dor, T. K. Rockwell, Y. Ben-Zion, Geological observations of damage asymmetry in the structure of the San Jacinto, San Andreas and Punchbowl faults in Southern California: A possible indicator for preferred rupture propagation direction. *Pure Appl. Geophys.* **163**, 301–349 (2006).
26. K. Aki, Maximum likelihood estimate of *b* in the formula  $\log N = a - bM$  and its confidence limits. *Bull. Earthquake Res. Inst. Univ. Tokyo* **43**, 237–239 (1965).
27. Y. Ben-Zion, Collective behavior of earthquakes and faults: Continuum-discrete transitions, progressive evolutionary changes, and different dynamic regimes. *Rev. Geophys.* **46**, RG4006 (2008).
28. M. T. Page, D. Alderson, J. Doyle, The magnitude distribution of earthquakes near Southern California faults. *J. Geophys. Res.* **116**, B12309 (2011).
29. D. R. Shelly, W. L. Ellsworth, D. P. Hill, Fluid-faulting evolution in high definition: Connecting fault structure and frequency-magnitude variations during the 2014 Long Valley Caldera, California, earthquake swarm. *J. Geophys. Res.* **121**, 1776–1795 (2016).
30. D. R. Shelly, S. C. Moran, W. A. Thelen, Evidence for fluid-triggered slip in the 2009 Mount Rainier, Washington earthquake swarm. *Geophys. Res. Lett.* **40**, 1506–1512 (2013).

31. A. A. Allam, Y. Ben-Zion, Seismic velocity structures in the southern California plate-boundary environment from double-difference tomography. *Geophys. J. Int.* **190**, 1181–1196 (2012).
32. D. Zigone, Y. Ben-Zion, M. Campillo, P. Roux, Seismic tomography of the Southern California plate boundary region from noise-based Rayleigh and Love waves. *Pure Appl. Geophys.* **172**, 1007–1032 (2015).
33. J. McGuire, Y. Ben-Zion, High-resolution imaging of the Bear Valley section of the San Andreas fault at seismogenic depths with fault-zone head waves and relocated seismicity. *Geophys. J. Int.* **163**, 152–164 (2005).
34. H. Fang, H. Zhang, H. Yao, A. Allam, D. Zigone, Y. Ben-Zion, C. Thurber, R. D. van der Hilst, A new algorithm for three-dimensional joint inversion algorithm of body-wave and surface wave data and its application to the Southern California plate boundary region. *J. Geophys. Res.* **121**, 3557–3569 (2016).
35. F. Waldhauser, W. L. Ellsworth, A double-difference earthquake location algorithm: Method and application to the northern Hayward fault, California. *Bull. Seismol. Soc. Am.* **90**, 1353–1368 (2000).
36. Y. Ben-Zion, S. Katz, P. Leary, Joint inversion of fault zone head waves and direct P arrivals for crustal structure near major faults. *J. Geophys. Res.* **97**, 1943–1951 (1992).
37. M. A. Lewis, Y. Ben-Zion, J. McGuire, Imaging the deep structure of the San Andreas Fault south of Hollister with joint analysis of fault-zone head and direct P arrivals. *Geophys. J. Int.* **169**, 1028–1042 (2007).
38. C. Thurber, H. Zhang, F. Waldhauser, J. Hardebeck, A. Michael, D. Eberhart-Phillips, Three-dimensional compressional wavespeed model, earthquake relocations, and focal mechanisms for the Parkfield, California, region. *Bull. Seismol. Soc. Am.* **96**, S38–S49 (2006).
39. E. O. Lindsey, V. J. Sahakian, Y. Fialko, Y. Bock, S. Barbot, T. K. Rockwell, Interseismic strain localization in the San Jacinto Fault Zone. *Pure Appl. Geophys.* **171**, 2937–2954 (2014).
40. A. Plesch, J. H. Shaw, W. A. Bryant, S. Carena, M. L. Cooke, J. F. Dolan, G. S. Fuis, E. M. Gath, L. B. Grant Ludwig, E. Hauksson, T. H. Jordan, M. Kamerling, M. R. Legg, S. C. Lindvall, H. Magistrale, C. Nicholson, N. A. Niemi, M. E. Oskin, S. C. Perry, G. Planansky, T. K. Rockwell, P. M. Shearer, C. C. Sorlien, M. P. Suss, J. Suppe, J. A. Treiman, R. S. Yeats, Community fault model (CFM) for southern California. *Bull. Seismol. Soc. Am.* **97**, 1793–1802 (2007).
41. V. Lyakhovskiy, Y. Ben-Zion, A. Agnon, Distributed damage, faulting, and friction. *J. Geophys. Res.* **102**, 27635–27649 (1997).
42. Y. Hamiel, V. Lyakhovskiy, A. Agnon, Poroelastic damage rheology: Dilation, compaction, and failure of rocks. *Geochem. Geophys. Geosyst.* **6**, Q01008A (2005).
43. Y. Ben-Zion, K. A. Dahmen, J. T. Uhl, A unifying phase diagram for the dynamics of sheared solids and granular materials. *Pure Appl. Geophys.* **168**, 2221–2237 (2011).
44. W. Thatcher, D. P. Hill, Fault orientations in extensional and conjugate strike-slip environments and their implications. *Geology* **19**, 1116–1120 (1991).
45. D. Kilb, A. M. Rubin, Implications of diverse fault orientations imaged in relocated aftershocks of the Mount Lewis, M<sub>L</sub> 5.7, California, earthquake. *J. Geophys. Res.* **107**, ESE 5-1–ESE 5-17 (2002).
46. M. W. Hamburger, K. Shoemaker, S. Horton, H. DeShon, M. Withers, G. L. Pavlis, E. Sherrill, Aftershocks of the 2008 Mt. Carmel, Illinois, Earthquake: Evidence for conjugate faulting near the termination of the Wabash Valley Fault System. *Seismol. Res. Lett.* **82**, 735–747 (2011).
47. S. Xu, Y. Ben-Zion, Numerical and theoretical analyses of in-plane dynamic rupture on a frictional interface and off-fault yielding patterns at different scales. *Geophys. J. Int.* **193**, 304–320 (2013).
48. Southern California Earthquake Data Center (SCEDC) (California Institute of Technology, 2013); 10.7909/C3WD3xH1.
49. J. L. Hardebeck, P. M. Shearer, A new method for determining first-motion focal mechanisms. *Bull. Seismol. Soc. Am.* **92**, 2264–2276 (2002).
50. Z. Peng, P. Zhao, Migration of early aftershocks following the 2004 Parkfield earthquake. *Nat. Geosci.* **2**, 877–881 (2009).
51. A. A. Holland, Earthquakes triggered by hydraulic fracturing in south-central Oklahoma. *Bull. Seismol. Soc. Am.* **103**, 1784–1792 (2013).

**Acknowledgments:** We thank H. Kanamori for helpful discussions. We also thank D. Shelly and an anonymous reviewer for their constructive comments. Figures were produced with the Generic Mapping Tools. **Funding:** The study was supported by the NSF (grants EAR-1550704 and EAR-1551411), by the U.S. Geological Survey (USGS)/National Earthquake Hazards Reduction Program (NEHRP) (grants G15AP00095 and G16AP00147), and by the Southern California Earthquake Center, which was funded by NSF Cooperative Agreement EAR-1033462 and USGS Cooperative Agreement G12AC20038. **Author contributions:** Z.E.R. performed template matching and derived the aftershock locations. E.H. relocated the templates and calculated the focal mechanisms. Z.E.R., E.H., and Y.B.-Z. contributed to the analysis and wrote the article. **Competing interests:** The authors declare that they have no competing interests. **Data and materials availability:** All of the raw waveform data are publicly available from the Incorporated Research Institutions for Seismology (IRIS) and the Southern California Earthquake Data Center. SCSN data were provided by the California Institute of Technology/USGS SCSN (doi: 10.7914/SN/CI) and the Southern California Earthquake Center (doi: 10.7909/C3WD3xH1). All other data needed to evaluate the conclusions in the paper are present in the paper and/or the Supplementary Materials. Additional data related to this paper may be requested from the authors.

Submitted 16 August 2016

Accepted 9 February 2017

Published 15 March 2017

10.1126/sciadv.1601946

**Citation:** Z. E. Ross, E. Hauksson, Y. Ben-Zion, Abundant off-fault seismicity and orthogonal structures in the San Jacinto fault zone. *Sci. Adv.* **3**, e1601946 (2017).